MATERIALS SCIENCE

Ultrafast solid-liquid intercalation enabled by targeted microwave energy delivery

Ming-Jian Zhang[1,2], Yandong Duan[1,2,3], Chong Yin[2,4], Maofan Li[1], Hui Zhong[5], Eric Dooryhee[6], Kang Xu[7]*, Feng Pan[1]*, Feng Wang[2]*, Jianming Bai[6]*

In chemical reactions, the breaking and formation of chemical bonds usually need external energy to overcome the activation barriers. Conventional energy delivery transfers energy from heating sources via various media, hence losing efficiency and inducing side reactions. In contrast, microwave (MW) heating is known to be highly energy efficient through dipole interaction with polar media, but how exactly it transmits energy to initiate chemical reactions has been unknown. Here, we report a rigorous determination of energy delivery mechanisms underlying MW-enabled rapid hydrothermal synthesis, by monitoring the structure and temperature of all the involved components as solid-liquid intercalation reaction occurs using in situ synchrotron techniques. We reveal a hitherto unknown direct energy transmission between MW irradiation source and the targeted reactants, leading to greatly reduced energy waste, and so the ultrafast kinetics at low temperature. These findings open up new horizons for designing material synthesis reactions of high efficiency and precision.

INTRODUCTION

Modern materials science evolves around the new materials available from synthetic chemistry, while how efficiently the desired structure can be obtained in short time scale is of paramount importance (*1*). Essentially, all synthesis reactions follow specific dynamic pathways with activation barriers associated with the highly unstable transition states. To overcome these barriers, atomic rearrangement always requires the energy assistance from the environment. Conventional energy supply is realized via combustion or electric heating of the reaction mixture, where energy from the heating sources is transferred to an intermediate media—atmospheric air or inert gas, reaction vessel or any solvent, which subsequently dissipates the energy to the targeted reactants, and the environment and nontargets (*2*–*5*). This energy transfer mode not only is inefficient and wasteful due to the disordering and nondirectional characteristics of all molecular/lattice thermal vibrations involved but also induces numerous undesirable side reactions.

An ideal energy transfer mode should be target oriented, which goes precisely from the heating source to the targeted reactants, and only activates the chemical bonds necessary for the formation of final products, such as electron and photon transfer in electrochemical and photon energy. The former, when applied in chemical reactions, is usually known as electrochemistry and can directly add/extract the electrons to/from certain reactants, forming the targeted chemical bonds through redox reactions. Having been extensively applied in the synthesis of various organic compounds and nanoparticles with notably enhanced electron economy and efficiency (*6*–*9*), the applicability of electrochemistry, however, is subject to restrictions of electron accessibility of all involved species, which is hard to satisfy for nonconductive and condensed matters, particularly solid-state and inorganic materials such as ceramics, ferroelectric, thermoelectric, superconductor, and topological insulators. The flashing sintering is exceptionally target oriented as the dc electric field is directly applied on grain boundaries (*10*, *11*). Similarly, photon energy has also been extensively applied in chemical reactions, the most well-known example of which is photosynthesis carried out by nature in plants that uses photons from the sunlight to precisely produce organic nourishments from CO_2 and water (*12*–*14*). Tremendous efforts have been devoted to extending the photosynthesis to various organic compounds via various photosensitizers and photocatalysts (*15*–*17*), but again, this highly accurate energy delivery cannot be applied to condensed matters, because ultraviolet-visible–infrared photons are usually of low power (10^{-3} to 10^{2} W) and low transmittance (10^{-3} to 10^{-1} m), which can hardly deliver energy into the bulk of the solid-state reactants.

Microwave (MW), a unique member of the photon energy forms, has the characteristics of good directionality, high transmittance (up to several meters), and high power (up to 10^{5} W) (*18*, *19*), which enable it to penetrate the bulk of condensed matters and drive the synthesis of solid-state inorganic materials in a highly efficient heating manner and with fast heating rate. Examples of the wide spectrum of materials synthesized via MW include organics (*20*–*23*), ceramics (*24*, *25*), alloys (*26*, *27*), metal organic frameworks (*28*), nanocatalysts (*29*), dielectric materials (*30*), thermoelectric materials (*31*), and ferroelectric materials (*32*), where spectacular accelerations, high yields, and high product purities under relatively mild conditions have all been reported (*20*–*23*). In general, MW irradiation could directly transmit its energy through the dipole moment of the asymmetric molecules/radicals and the magnetic moment of the magnetic ions (*33*), which converts electromagnetic energy into heat. Consequently, direct energy delivery into the bulk of the condensed matter via resonance of the polar molecular and unpaired electrons could occur without going through the slow dissipation from surface to bulk, as it does in conventional heating (*34*). Direct impact of MW irradiation on the oxygen sublattice in the bulk structure was revealed

[1]School of Advanced Materials, Peking University, Shenzhen Graduate School, Shenzhen 518055, People's Republic of China. [2]Sustainable Energy Technologies Department, Brookhaven National Laboratory, Upton, NY 11973, USA. [3]School of Science, Hebei University of Science and Technology, Shijiazhuang 050018, People's Republic of China. [4]Ningbo Institute of Materials Technology and Engineering, Chinese Academy of Sciences, Ningbo 315201, People's Republic of China. [5]Joint Photon Sciences Institute, Stony Brook University, Stony Brook, NY 11790-2100, USA. [6]National Synchrotron Light Source II, Brookhaven National Laboratory, Upton, NY 11973, USA. [7]US Army Research Laboratory, Energy Storage Branch, Sensor & Electron Devices Directorate, Adelphi, MD 20783, USA.
*Corresponding author. Email: conrad.k.xu.civ@mail.mil (K.X.); panfeng@pkusz.edu.cn (F.P.); fwang@bnl.gov (F.W.); jmbai@bnl.gov (J.B.)

recently in an in situ pair distribution function (PDF) study (*35*). Nevertheless, in most of the actual MW synthesis practices (*36*, *37*), energy is still absorbed by the reaction vessels or other media in the form of heat, which, in turn, dissipates to the raw reactants via conventional heat conduction. Namely, the direct energy delivery from MW to chemical bonds has not been realized in these cases.

Metal oxides are arguably the most important solid materials in various applications because they are naturally abundant and exhibit numerous structures and properties of significance to optics, electronics, magnetism, catalysis, and energy conversion/storage fields (*38*–*42*). Notably, since the first report of $LiCoO_2$ in 1980s, lithium transition metal (TM = Ni, Co, Mn) layered oxides have been nurtured into a promising cathode material family for Li-ion batteries (LIBs) due to their unique intercalation chemistries with Li^+ (*43*–*45*). Solid-state reaction, using the mixture of a Li source (LiOH or Li_2CO_3) and TM precursors (coprecipitated Ni-Mn-Co hydroxides or carbonates), is the mainstream synthesis of these layered oxides in both laboratory research and industrial production (*46*–*49*). The formation of desirable TM layered structures requires high temperature (750° to 1000°C), long reaction duration time (>10 hours), and heavy carbon footprint, which lead to enormous energy consumption, environmental pollution, and high production cost. New synthetic methods of lower cost, shorter reaction duration, and minimized energy consumptions would be of critical importance considering the already gigantic (in billion dollars) but still rapidly increasing scale of these LIB materials needed by the future energy storage markets.

Here, we adopt the synthesis of TM layered oxide $LiNi_{1/3}Mn_{1/3}Co_{1/3}O_2$ (NMC333) as a model reaction to explore the possibility of precise energy delivery from MW irradiation to the reactants so that the targeted structures can be efficiently assembled with minimum energy dissipation to the environments and nontargets. Time-resolved synchrotron x-ray diffraction (TRS-XRD) as a powerful in situ probe was used to monitor the entire progress of forming the layered oxides, where the MW effect on both external environment and individual reactants was rigorously and quantitatively evaluated. As references, classic thermal syntheses of NMC111, including conventional solid-state and hydrothermal, were also studied using TRS-XRD. Our analysis reveals that, by proper selection of the reaction vessel and solvent, MW energy could be directly and precisely guided to the reactant particles/ions, i.e., TM hydroxide and hydrated Li^+. The confined energy instantly accumulated and drove an ultrafast formation of layered oxide structures in less than 4 min, at a rather low temperature (<160°C), in contrast to the long duration (hours) and high temperature (up to 1000°C) needed for the conventional calcination. The identification of this hitherto unknown energy transmission mechanism not only enables molecular-level understanding of how energy transfers in MW synthetic chemistry but also opens up a new perspective to design and synthesize new materials with unprecedented high energy efficiency and chemical accuracy.

RESULTS AND DISCUSSION

Real-time tracking of intercalation reaction in MW hydrothermal synthesis

Figure 1A illustrates the experimental setup of TRS-XRD for the in situ MW hydrothermal synthesis. The x-ray powder diffraction (XPD) beamline (28-ID-2) in the National Synchrotron Light Source-II (NSLS-II) at Brookhaven National Laboratory, with the produced ultrahigh flux, allows us to track the fast kinetics during the MW hydrothermal synthesis. An in situ MW reactor was developed, with special cell design that meets requirements of MW transparent, chemically inert, and high mechanical strength against high internal pressure (described in Materials and Methods; fig. S1). With the in-house developed reactor, TRS-XRD was successfully performed, where the structural evolution during the entire synthesis from hydroxide precursors to the final layered oxide can be closely tracked and quantitatively analyzed. The cell design developed here has obvious advantages of not only tracking reactions but also monitoring the local heat dissipation that is crucial to fundamental understanding of the energy delivery mechanisms.

Reaction kinetics of intercalation reaction in MW hydrothermal synthesis

The reaction of NMC333 from its TM hydroxide precursor (NMCOH, *P*-3*m*1) with LiOH is a topotactic reaction involving Li^+ intercalation into a solid lattice, in which the layered lattice structure is retained while taking Li^+ in between the TM layers and accompanying the interlayer sliding of neighboring TM layers (*50*). As shown in Fig. 1B, under MW irradiation, the intercalation reaction

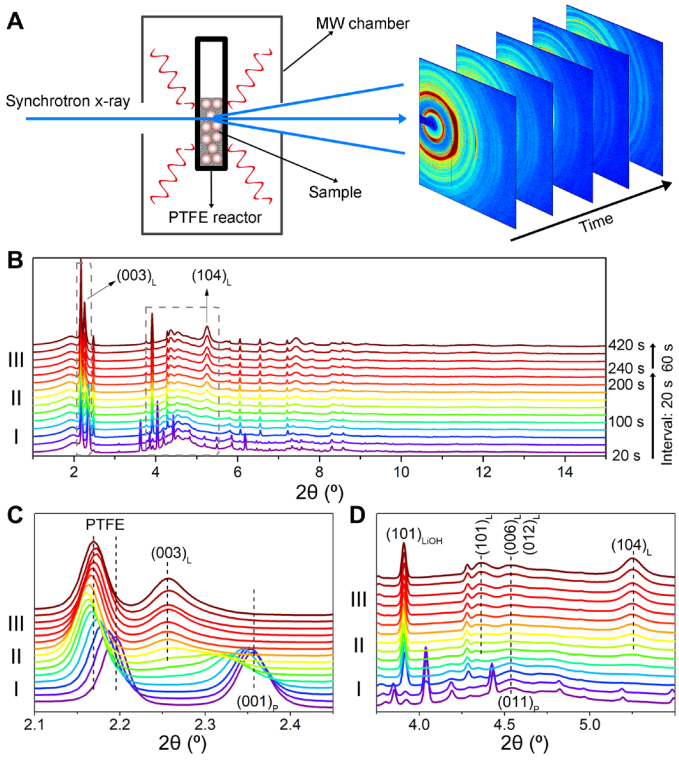

Fig. 1. Real-time monitoring of structural evolution during MW hydrothermal synthesis. (**A**) Schematic illustration of the experimental setup, with a PTFE-based reactor specialized for fast synchrotron x-ray probing of the MW hydrothermal synthesis (left) and representative 2D diffraction patterns taken during synthesis of the layered oxide NMC333 (right). The synchrotron x-ray wavelength is 0.1885 Å. (**B**) TRS-XRD patterns recorded during in situ MW hydrothermal synthesis of NMC333. (**C**) Enlarged regions in the 2θ range of 2.10° to 2.45° [marked by a gray dashed rectangle in (A) to show the evolution of the $(001)_P$ peak associated with the hydroxide precursor and the $(003)_L$ peak of the layered oxide]. (**D**) Enlarged region in the 2θ range of 3.75° to 5.50° [marked by a gray dashed rectangle in (A)] to show the evolution of $(104)_L$ and other peaks associated with the layered oxide.

is observed through the apparent change of TRS-XRD patterns from hydroxide precursor to the layered oxide. More details are revealed by the zoom-in view of the two selected regions. The main peak of polytetrafluoroethylene (PTFE) shifts to lower angles with time, hinting a thermal effect under MW irradiation (Fig. 1C). In the first 80 s, $(001)_P$ peak of the precursor gradually shifts to lower angles, while its intensity decreases with time, indicating the increase of the interplanar spacing but the decrease of the ordering, which results from the thermal effect and Li^+ insertion. Until 100 s, $(003)_L$ peak of layered phase appears, which subsequently experiences a rapid increase and displays a reversed trend compared to the $(001)_P$ peak, indicating the growth of the layered phase at the expense of the hydroxide precursor. As shown in Fig. 1D, $(104)_L$ peak also appears at 100 s, following a similar trend as $(003)_L$ peak; meanwhile, $(011)_P$ disappears and $(101)_L$ and $(006)_L/(012)_L$ appear and grow with time, which further confirms the completion of the intercalation of solvated Li^+ into NMCOH lattice.

Quantitative analysis is performed by tracking the evolution of the main peaks of PTFE, hydroxide precursors, and layered oxides. First, the temperature profile was determined by using PTFE as an internal standard (described in Materials and Methods; fig. S2 and tables S1 and S2). As shown in fig. S3A, the temperature of the reaction vessel rapidly increases to 160°C in the first 150 s and then drops to ~125°C, remaining constant during the rest of the reaction. Then, the positions and areas of the characteristic peaks, including $(001)_P$ of the precursor and $(003)_L$ and $(104)_L$ of the layered oxide, were tabulated in table S3 and plotted as a function of time in fig. S3B and Fig. 2B. The whole process could be divided to three regions: (i) region I (0 to 100 s), where only the precursor with initial Li^+ insertion mentioned above can be detected; (ii) region II (100 to 200 s), where phase transformation occurs, and $(003)_L$ and $(104)_L$ peaks for the layered oxide continuously shift to larger *d* spacing with growing intensities, indicating further Li^+ insertion into the layered phase; and (iii) region III (after 200 s), where the peak positions of $(003)_L$ and $(104)_L$ nearly approach a constant level, while their intensities increase abruptly with time, revealing the rapid propagation of the crystalline phase. In short, the intercalation reaction is initialized at a temperature below 160°C during the first 100 s and completed within 200 s. The entire reaction only took less than 4 min at temperatures below 160°C.

The reaction kinetics can be evaluated through the content decrease of precursor, represented by the peak areas of $(001)_P$. Because the first two regions are not isothermal (with temperature varying in the range of 135° to 155°C as shown in fig. S3A), the increase of $-\ln(I(001)_t/I(001)_0$ is not linear in Fig. 2C [wherein $I(001)_0$ and $I(001)_t$ are the peak areas of $(001)_P$ at the time of 0 min and *t* min, respectively]. The reaction rate *K* is calculated using the mean value theorem of integrals (described in Materials and Methods, table S4), with a mean value of 1.819 min^{-1}, which is one order of magnitude higher than that of the traditional hydrothermal and solid-state reactions (as discussed below). To our best knowledge, such an ultrafast kinetics for solid-liquid reactions has never been reported.

Low-temperature and ultrafast intercalation reaction of MW hydrothermal synthesis

To compare the reaction kinetics of MW hydrothermal synthesis with those of the conventional hydrothermal and solid-state syntheses, TRS-XRD measurements were also applied to the latter two, with similar analysis performed (Fig. 3, A and B, and figs. S4 to S7).

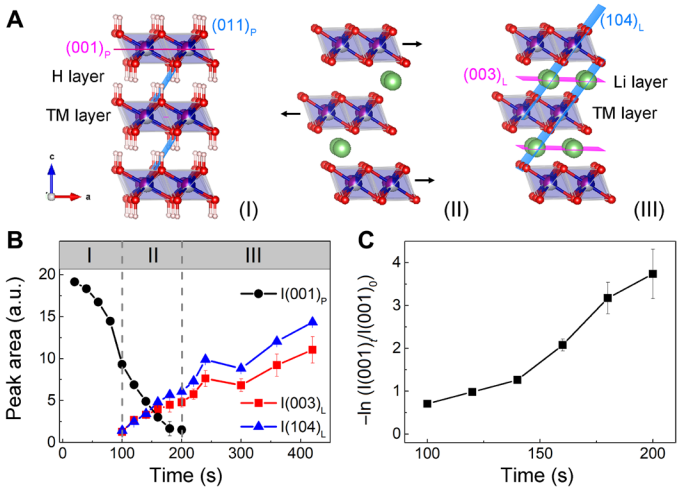

Fig. 2. MW-enabled ultrafast intercalation reaction during hydrothermal synthesis of layered oxide. (**A**) Schematic illustration of the intercalation reaction from hydroxide precursor (space group *P*-3*m*1, the left panel I) to layered oxide (space group *R*-3*m*, the right panel III), indicating a topotactic reaction that preserves the layered framework while undergoing H^+ extraction/Li^+ insertion and interlayer sliding between neighboring TM layers (the middle panel II). (**B**) Evolution of the integrated peak area of $(001)_P$, $(003)_L$, and $(104)_L$ [associated with the hydroxide precursor and the layered oxide; denoted as $I(001)_P$, $I(003)_L$, and $I(104)_L$, respectively] with time, showing three regions of the phase transformation, I, II, and III (as labeled). a.u., arbitrary units. (**C**) Phase transformation as a function of the time (*t*). Here, $-\ln(I(001)_t/I(001)_0)$ is used to monitor the content decrease of precursor phase, wherein $I(001)_0$ and $I(001)_t$ are the peak areas of $(001)_P$, at the time of 0 min and *t* min, respectively.

As shown in Fig. 3 (A and B), it takes about 22 and 30 min, respectively, for those syntheses to complete the same degree of phase transformation, which are four and six times longer than the MW hydrothermal synthesis, respectively, while the temperatures required are 160° and 302°C, respectively. The reaction rates *K* of conventional hydrothermal and solid-state synthesis are determined as 0.096 (at 160°C) and 0.091 (at 302°C), an order of magnitude smaller than that of the MW hydrothermal synthesis (1.819 min^{-1}). Similar hydrothermal syntheses were performed at 150° and 170°C, and similar solid-state syntheses were performed at 293° and 311°C. All *K* values are summarized in Fig. 3C and table S4, further confirming a much faster kinetics being enabled at a much lower environment temperature under MW irradiation. In addition, the morphology of the spherical secondary particle is maintained after MW hydrothermal and conventional hydrothermal syntheses (fig. S8).

During the reaction process, the framework transforms from a *P*-3*m*1 symmetry to an *R*-3*m* symmetry (Figs. 1B and 2A), with an increase of the lattice parameter *c* from 4.58 to 4.78 Å. Therefore, the change in *c* of NMCOH can serve as an indicator of the extent of Li^+ insertion during the MW hydrothermal (red curve), conventional solid-state (black curve), and conventional hydrothermal syntheses (as shown in Fig. 3D). The *c* values of NMCOH in its water suspension under MW irradiation in the absence of LiOH are also plotted (green curve) as the reference to calibrate the pure thermal expansion effect. The curves of the *c* values for conventional solid-state and hydrothermal synthesis are overall overlapped below 100°C, indicating the dominant thermal expansion with no or only negligible Li^+ insertion. Above 100°C, a very small amount of Li^+ insertion may occur in these two cases (hinted by the slightly higher locations

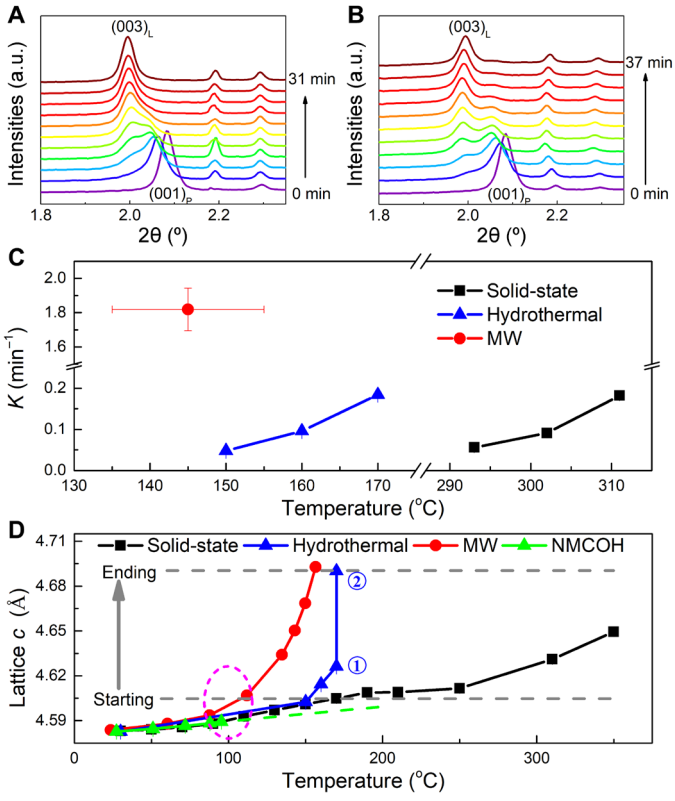

Fig. 3. Ultrafast reaction kinetics of MW hydrothermal synthesis against conventional hydrothermal and solid-state syntheses. (**A**) TRS-XRD patterns during the in situ hydrothermal synthesis of NMC333 at 160°C. (**B**) TRS-XRD patterns during the in situ solid-state synthesis of NMC333 at 302°C. (**C**) Comparison of the reaction rates *K* for MW hydrothermal synthesis (red) with that for the solid-state syntheses (at 293°, 302°, and 311°C; blue) and the hydrothermal syntheses (at 150°, 160°, and 170°C; black). Details of the calculation of *K* values can be found in figs. S5 and S6. (**D**) Lattice parameter *c* of the hydroxide precursor NMCOH as a function of the temperature during solid-state synthesis (black), hydrothermal synthesis (blue), and MW hydrothermal synthesis (red). It serves as an indicator to track the extent of Li^+ insertion into the precursor. The two dashed gray horizontal lines are used to represent the starting and ending points for the phase transformation, which are defined as the time point when the $(003)_L$ peak of the layered oxide was initially observed and the $(001)_P$ peak of the precursor completely disappeared, respectively. The last two points in the blue curve, marked by ① and ②, are recorded when holding at 170°C for 0 and 12 min, respectively. The initial difference between MW and other cases is highlighted by the magenta ellipse, hinting that Li insertion occurred below 100°C. The green curve was obtained during MW irradiation on NMCOH in its water suspension in the absence of LiOH, representing the pure thermal expansion of NMCOH. The green dashed line is extrapolated from the data points below 100°C based on the linear thermal expansion of NMCOH.

of the black and blue curves than that of the green dashed line). In contrast, substantial Li^+ insertion already occurs below 100°C under MW irradiation (with the obvious trend that the red curve surpasses over the green curve as highlighted with a magenta ellipse). Moreover, under MW irradiation, the parameter *c* increases exponentially in the temperature range between 100° and 150°C in just 2 min, in sharp contrast against conventional hydrothermal (holding at 170°C for 12 min) and solid-state syntheses, reflecting a much faster Li^+ insertion into the TM layers of NMCOH. The increased Li-slab distance facilitates Li^+ movement with the reduced activation energy for Li^+ diffusion (*51*–*55*), which accelerates the Li^+ transport from the surface to the bulk in the TM oxide framework. In Fig. 3D, *c* values at the starting (around 4.61 Å) and ending points (4.69 Å) remain similar for MW hydrothermal and conventional hydrothermal reactions, implying that a similar reaction pathway was followed. Solid-state reaction differs from these two, with much smaller *c* value (4.65 Å) when completing the phase transformation at 350°C, representing a much less Li^+ insertion before the structural phase transformation is completed. This difference should be related to the different forms of Li^+, i.e., LiOH maintains its solid form in solid-sate synthesis, while solvated Li^+ prevails in both MW and conventional hydrothermal reactions.

Energy delivery mechanism underlying MW-enabled synthesis

To estimate the energy delivery to individual components involved in the synthesis, XRD patterns were taken from empty PTFE tube and PTFE tube filled with water, saturated LiOH aqueous solution, and NMCOH suspension, respectively, as they are heated up with MW irradiation under a constant power. The corresponding temperature curves are deduced from the thermal expansions of PTFE (fig. S9) and presented in Fig. 4A, together with the temperature curve recorded during the in situ MW hydrothermal synthesis (gray curve) for comparison. Except the gray curve, all other curves show the similar trend—the temperature increases rapidly in the first 250 s and then approaches a constant value after 300 s, implying that heat equilibrium is achieved. At 300 s, the temperatures of the empty PTFE tube and the tube filled with water, saturated LiOH aqueous solution, and NMCOH suspension rise from room temperature (23°C) to 50°, 60°, 68°, and 96°C, respectively. To quantitatively evaluate the MW-absorbing ability of different species, we calculated the heat converted by water, LiOH, and NMCOH from MW, respectively, by combining our experimental data with the specific heats (described in Materials and Methods) (*56*). As summarized in table S6 and Fig. 4B, the heat converted by a mole of LiOH and NMCOH is 5.0 and 8.3 times higher than that of water, respectively. This demonstrates that MW energy can bypass water and the PTFE tube wall and is directly absorbed by LiOH and NMCOH, which then plays the dominant role in heating up the system. Namely, hydrated Li^+ ions and NMCOH excited by MW dielectric and magnetic interactions, respectively (*57*–*60*), may have higher kinetic energy than what the apparent temperature indicates. It has been confirmed by the comparison of the heating rates for four cases in Fig. 3C.

During the in situ MW synthesis, the highest temperature of around 160°C is achieved in only 3 min (gray curve of Fig. 4A). Such a rapid temperature increase results from the combined MW absorption by PTFE tube, H_2O, hydrated Li^+ ions, and NMCOH. Note the system temperature drops starting from 160 s, which accompanies the phase transformation process in region II (Fig. 2B). This apparent deviation from the Arrhenius law is due to the inhomogeneous temperature or local kinetic energy distribution. In other words, a part of MW energy directly interacts with NMCOH and hydrated Li^+ to reduce the activation energy E_a of Li^+ insertion and accelerates the phase transformation, instead of conversion into heat (*61*). The energy delivery pathway apparently differs from MW solid-state syntheses that used ceramic crucibles (*36*, *37*) or from the MW solvothermal syntheses that used solvents such as ethylene glycol. In either case, the MW energy has to be absorbed by either reaction vessel or the solvent molecule as an intermediate medium (*62*, *63*), before they transfer heat to the reactants.

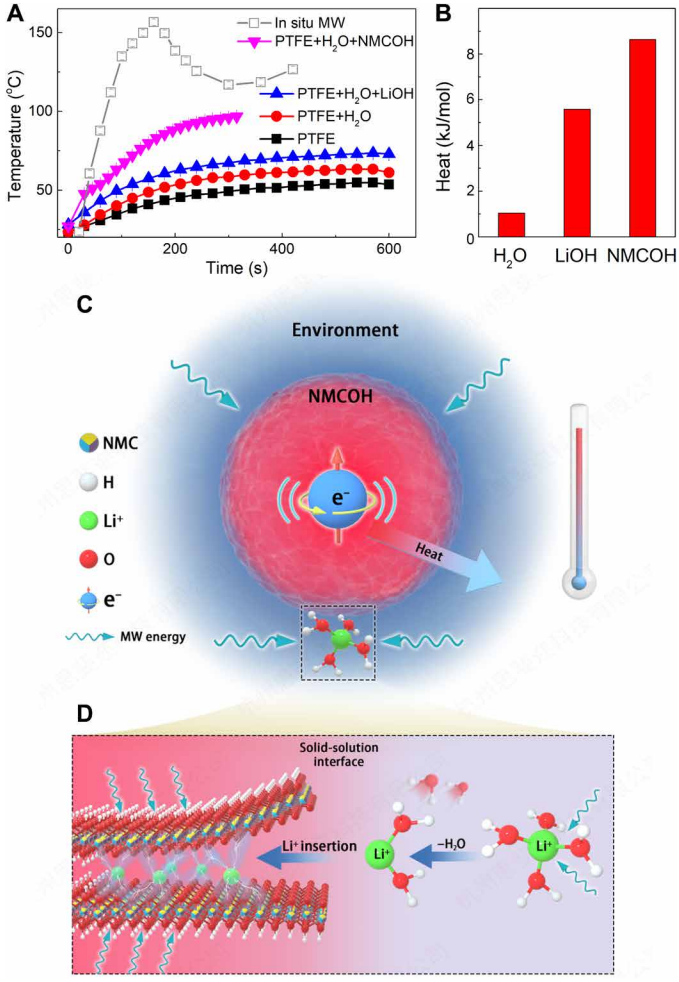

Fig. 4. Mechanism of targeted energy delivery underlying MW-enabled rapid synthesis. (**A**) Temperature curves of an empty PTFE tube (black; labeled as PTFE), a PTFE tube with water (red; labeled as PTFE + H_2O), a PTFE tube with LiOH solution (blue; labeled as PTFE + H_2O + LiOH), and a PTFE tube with TM hydroxide precursor (NMCOH) suspension (magenta; labeled as PTFE + H_2O + NMCOH) under MW irradiation as derived from the corresponding in situ MW experiments shown in fig. S9. The temperature curve during in situ MW synthesis (gray; labeled as in situ MW) from fig. S3A was also plotted for comparison. (**B**) Estimated heat absorption by H_2O, LiOH, and NMCOH under the same MW irradiation, to compare their MW absorption capability. (**C**) Schematic illustration to show the energy delivery pathways during the MW hydrothermal synthesis. The spinning electron represents the intensive magnetic interaction between NMCOH particle and MW irradiation, which produces a great amount of heat, conducting from NMCOH particles to the environment. (**D**) Schematic illustration to show that the accelerated Li^+ insertion process occurred at the solid-solution interface, due to the strong dielectric and magnetic interactions of the MW with hydrated Li^+ ions and magnetic TM cations (Co^{2+} $3d^7$ and Mn^{2+} $3d^5$), which leads to the ultrafast phase transformation.

On the basis of the discussion above, an energy delivery mechanism is schematically depicted for the ultrafast intercalation reaction enabled by MW irradiation (Fig. 4, C and D). Different from the traditional indirect energy delivery pathway, the MW energy is precisely guided toward the reactants, i.e., NMCOH particle and hydrated Li^+ $[Li^+(H_2O)_4]$, whose magnetic/dielectric properties (namely, the unpaired electrons and the dipole moment, respectively) allow them to take precedence before solvent (water) or reaction vessel (PTFE) accepts the energy. In the perspective from chemical kinetics, this direct energy delivery leads to instantaneous accumulation of kinetic energy for these targeted molecules, assisting them to achieve activated states. The effective collisions of these activated species at the confined solid-solution interface result in the rapid completion of intercalation reaction at a low environmental temperature (Fig. 4C). The reaction pathway occurring on the molecular level at the solid-solution interface (black dashed rectangle) between NMCOH particle and hydrated Li^+ is illustrated in Fig. 4D. First, LiOH dissolves in deionized water to produce high-concentration $[Li^+(H_2O)_4]$ (*64*–*66*). The dielectric interaction with MW brings very high kinetic energy to $[Li^+(H_2O)_4]$, partially desolvating it from the coordinated water molecules. The resultant hydrated $[Li^+(H_2O)_{4-x}]$ will be stabilized through coordination with O anions exposed at the surface of NMCOH particles, while the instant high kinetic energy helps them overcome the energy barrier for Li^+ to enter the lattice of NMCOH. This Li^+ insertion process during the synthesis is similar to what occurs during the electrochemical process (*67*, *68*). Meanwhile, NMCOH particles, with even higher kinetic energy due to the stronger magnetic interaction of TM cations with the incident MW irradiation, form a temperature gradient at the solid-solution interface, further facilitating Li^+ insertion. Here, the magnetic and dielectric interactions between MW and NMCOH particle and hydrated Li^+ precisely guided MW energy to overcome the activation energy barriers, leading to ultrafast Li^+ insertion kinetics at the solid-solution interface and consequently an ultrafast phase transformation. In comparison with the conventional energy delivery modes during hydrothermal and solid-state synthesis, this targeted energy utilization greatly reduces energy waste in the form of heat.

As viewed from the Arrhenius equation $K = Ae^{-Ea/BT}$, MW energy directly activates the targeted reactants, which increases the probability of the local synthesis reaction via preexponential factor A, and the reaction can thus be completed with a higher rate K even at a lower temperature T (*69*–*71*). In the previous studies as reported so far, researchers have not been able to accurately monitor the MW synthesis reaction in real time, which may explain the inconsistent results and therefore the debate on the causes for the observed reaction rate enhancements and the existence of the specific MW effects. Here, the findings of the targeted energy delivery from the systemic in situ synchrotron x-ray studies lay a physical foundation for explaining the MW-enabled ultrafast hydrothermal synthesis.

In this study, by developing an in situ MW reactor that allows real-time tracking of chemical reactions, we reveal a previously undiscovered mechanism of energy delivery in the MW hydrothermal reaction. With rigorous characterization and quantitative analysis during the intercalation reaction aiming to prepare a representative TM layered oxide NMC333, we describe how the energy carried by the incident MW irradiation is directly received by the targeted reactants (hydrated Li^+ and TM hydroxide particles) with negligible interception by the reaction medium (water and reaction vessel). This direct energy delivery is responsible for the ultrafast reaction kinetics (<4 min) at mild temperature (<160°C). Compared with the requirements of long time and/or high temperatures in conventional hydrothermal and solid-state reactions, this much higher efficiency in completing the same reaction is beyond doubt of critical importance for synthetic chemistry of condensed matters. The discovery from this study opens up new prospects to the design of materials and chemistries that benefit from precise and highly targeted energy delivery.

MATERIALS AND METHODS

Design of the MW reactor and in situ cell for MW hydrothermal synthesis

We modified a household MW oven (JEM3072DH/SH, General Electric Company) for in situ XRD measurement by cutting a round hole (50 cm in diameter) on the top of the MW chamber and covering it with a piece of aluminum shim stock of 0.005 inch on top of a Kapton sheet with the same thickness. The MW oven was mounted at the beamline with the hole facing the detector (fig. S1A). This acts as a window for scattered x-ray while effectively shielding the MW radiation from leaking out of the chamber. Two holes with a diameter of 1 cm along the x-ray beam passage were made, one at the bottom of the chamber and the other on the aluminum shim stock, to avoid x-ray scattering from the metal walls. With the 2.45-GHz MW (12 cm in wavelength), the leakage was tested to be below the limit set by federal standard 21 CFR 1030.10 (Code of Federal Regulations, Title 21, Volume 8, revised as of 1 April 2019). To conduct the TRS-XRD experiments, a control panel was wired to the MW oven with cables so that it can be operated from outside of the beamline hutch. The MW can only be turned on with the beamline hutch secured to ensure personnel safety.

In the past, various in situ x-ray diffraction experiments have been conducted at this facility on both solid-state and hydrothermal syntheses (*72*–*76*). However, the in situ cells developed therein are not suitable under MW irradiation. Therefore, a new in situ reactor needs to be designed, which must meet several requirements: (i) MW transparency; (ii) being chemically inert to all reactants; (iii) being free of any metal parts, which may produce electric arcs and damage the MW generator; and (iv) being airtightly sealed while withstanding pressures above 100 psi to contain the superheated solvent (water) under MW irradiation. Such a cell was created using PTFE tubes with inner and outer diameters of $^1/_{16}$ inch (ID) and $^1/_8$ inch (OD) (EW-06605-27, Cole-Parmer Inc.), which is MW transparent, is chemically inert, and has high mechanical strength against high internal pressure (fig. S1, B and C). It can be used in a wide temperature range of −240° to 260°C and withstand the maximum pressure (25.5 bar).

In a typical experiment, we loaded about 30 mg of the mixture into a PTFE tube with a length of 6 cm and injected 15 μl of deionized water as solvent. The tube was airtight sealed by PTFE rods ($^1/_{16}$ inch in diameter) and silicone caulk and fastened with poly ether ethera ketone (PEEK) low-pressure union and nuts (Cole Parmer Inc.) from both ends.

In situ MW hydrothermal synthesis experiments

Time-resolved high-energy XRD patterns were collected at Sector 28-ID-2 of the NSLS-II at Brookhaven National Laboratory. A two-dimensional (2D) x-ray detector was deployed to collect the XRD patterns. The focused beam size is 0.5 mm (horizontal) by 0.5 mm (vertical). Different wavelengths were adopted because multiple experiments were conducted at different dates.

The wavelength of x-ray beam for the in situ MW hydrothermal synthesis was 0.1885 Å. To ensure the success of the in situ MW experiment, much effort has been devoted to the ex situ experiments in our laboratory. Last, the optimal conditions were determined. In a typical experiment, the hydroxide precursor for $Li(Ni_{1/3}Mn_{1/3}Co_{1/3})O_2$ (denoted as NMC333) with nominal average composition of $Ni_{1/3}Mn_{1/3}Co_{1/3}(OH)_2$ was synthesized via a modified coprecipitation method. Then, each PTFE tube with a length of 6 cm was cut as a reactor. $Ni_{1/3}Mn_{1/3}Co_{1/3}(OH)_2$ (150 mg) and LiOH (150 mg) were thoroughly mixed by grinding for about 30 min. Then, 30 mg of the mixture was loaded into the tube and 15 μl of distilled water was further added. The tube was then airtight sealed and placed in the modified MW oven for the MW hydrothermal synthesis. One hundred percent of power was applied for 15 min. The XRD data were simultaneously recorded during the MW process with each scan for 30 s. The MW synthesis reaction and other MW thermal effect tests below are all conducted with constant MW power.

Temperature determination and the thermal effect for the MW hydrothermal synthesis

To determine the temperature profile during the in situ MW hydrothermal experiment, temperature-resolved heating experiments for the empty PTFE tube was performed to determine the thermal expansion coefficient. A Linkam TS 1500 furnace was deployed to heat the empty PTFE tube from 33° to 233°C in a heating rate of 5°C min^{-1}. The XRD patterns were simultaneously recorded during the heating process.

To study the MW thermal effect during the in situ MW hydrothermal experiment, MW heating experiments for the empty PTFE tube, the PTFE tube with H_2O, the PTFE tube with H_2O and LiOH (LiOH saturated solution), and the PTFE tube with H_2O (15 μl) and $Ni_{1/3}Mn_{1/3}Co_{1/3}(OH)_2$ (30 mg) were also performed using the same conditions as that during in situ MW hydrothermal synthesis. Time-resolved high-energy XRD patterns were collected at Sector 28-ID-2 of the NSLS-II. The wavelength of synchrotron x-ray beam is 0.1885 Å.

In situ hydrothermal synthesis experiments

To compare with the MW hydrothermal synthesis, the synthesis by the conventional hydrothermal method was also performed. $Ni_{1/3}Mn_{1/3}Co_{1/3}(OH)_2$ (150 mg) and LiOH (150 mg) were mixed thoroughly, and then about 30 mg of the mixture was added into a glass capillary reactor. Deionized water (15 μl) was also added as a solvent. Then, the reactor was placed into a vertical coil furnace. The reaction was performed at three different temperatures: 150°, 160°, and 170°C. High-energy XRD patterns were collected at Sector 28-ID-1 of the NSLS-II. The wavelength of the x-ray beam was 0.1667 Å. The temperature of the vertical coil furnace is precalibrated using ceria as thermal expansion standard.

In situ solid-state synthesis experiments

The precursor $Ni_{1/3}Mn_{1/3}Co_{1/3}(OH)_2$ was completely mixed with LiOH in a molar ratio of 1:1.05 by grinding for 1 hour. For temperature-resolved XRD measurements, the mixture was pressed into pellets with a thickness of around 1 mm and a diameter of 7 mm and then placed in a furnace (Linkam TS 1500) vertically, with the window perpendicular to the x-ray beam. The pellets were then heated to 850°C in air with a rate of 20°C min^{-1}. High-energy XRD patterns were collected at Sector 28-ID-2 of the NSLS-II. The wavelength of the x-ray beam was 0.23696 Å.

To determine the activation energy of the phase transformation during the solid-state synthesis, solid-state reactions were also performed at three different control temperatures: 320°, 330°, and 340°C. The corresponding calibrated temperatures are 293°, 302°, and 311°C, respectively. The mixture used here was the same with that during in situ MW hydrothermal synthesis and in situ conventional hydrothermal synthesis above. Time-resolved XRD were also collected. High-energy XRD patterns were collected at Sector 28-ID-1 of the NSLS-II. The wavelength of the x-ray beam was 0.1886 Å. The temperature of the furnace is precalibrated using ceria as thermal expansion standard.

Morphology characterizations

A Zeiss SUPRA-55 scanning electron microscope (SEM) was used to record SEM images for the hydroxide precursor, the products by the MW hydrothermal and the conventional hydrothermal method. The conventional hydrothermal synthesis was performed at 160°C for 24 hours.

Estimation of the reaction rate *K* based on the mean value theorem of integrals

For a first-order chemical reaction, the reaction rate can be formulated as

$$\frac{dC}{dt} = -KC \quad (1)$$

where C is the concentration of the reactant, t is the time, and K is the reaction rate constant, which can be derived from a linear equation in an isothermal reaction

$$-\ln\frac{C(t)}{C(0)} = Kt \quad (2)$$

For a non-isothermal reaction, the temperature-dependent reaction rate constant is a function of time; the mean value theorem of integrals can be applied to estimate the K value in a time period

$$\int_{t1}^{t2}\frac{dC}{C} = -\int_{t1}^{t2}K(t)\,dt = K(t_{\mathrm{mean}})\,(t2-t1) = -\ln\frac{C(t2)}{C(t1)} \quad (3)$$

where $K(t_{\mathrm{mean}})$ is the mean reaction rate between time $t1$ and $t2$ or between reaction temperature $T(t_1)$ and $T(t_2)$.

Using Eq. 3 and the data shown in Fig. 2C, K is estimated as 1.819 min^{-1} for the MW synthesis in the time period from 100 to 200 s.

Estimation of the heat converted by different species from MW irradiation

The heat converted by water, LiOH, and NMCOH from MW irradiation can be estimated, respectively, by combining the measured temperature rises of the system (Fig. 4A) with the specific heats of each component.

For water-filled PTFE tube, the heat needed for the temperature rise (23° to 60°C) in PTFE + H_2O (red curve in Fig. 4A) is given by

$$Q_{\mathrm{water}} = C_{\mathrm{water}}V_{\mathrm{water}}\Delta T_{\mathrm{water}} + C_{\mathrm{PTFE}}V_{\mathrm{PTFE}}\Delta T_{\mathrm{PTFE}}$$

Q_{water} is the heat converted by water, which accounts for all MW energy absorbed, as the MW absorption of the PTFE in this case is negligible. We also ignore the heat loss of the system to the surrounding in this equation. C_{water} and C_{PTFE} are the volume specific heats of water (4.182 J K^{-1} ml^{-1}) and PTFE (2.578 J K^{-1} ml^{-1}) (*77*). With the PTFE tube of $^1/_8$ inch OD and $^1/_{16}$ inch ID, the volume ratio of water and PTFE is 1:3 (e.g., V_{water} = 1 ml, V_{PTFE} = 3 ml). $\Delta T_{\mathrm{water}}$ and ΔT_{PTFE} are the temperature variations of water (37°C) and PTFE (10°C), respectively. Note here that we assume that the heat needed to increase the temperature of the PTFE tube from the room temperature to 50°C is from the hot air in the MW cavity and therefore is not included in the calculation. Thereby, Q_{water} is calculated as 0.232 kJ ml^{-1} or 4.18 kJ mol^{-1} based on the equation and the numerical values listed above.

Similarly, with knowledge of the specific heat of LiOH solution (C_{LiOH}, 2.071 J g^{-1} K^{-1}) and its solubility in water (12.8 g/100 ml at 20°C) (*78*, *79*), the volume specific heat of LiOH solution ($C_{\mathrm{Li\text{-}Sol}}$) is derived as 4.08 J K^{-1} ml^{-1}. Within the x-ray beam, the volume ratio of LiOH solution and PTFE is 1:3 ($V_{\mathrm{Li\text{-}Sol}}$:$V_{\mathrm{PTFE}}$ = 1:3). The temperature variations for solution and PTFE ($\Delta T_{\mathrm{Li\text{-}Sol}}$ and ΔT_{PTFE}) are 45° and 18°C, respectively, as the temperature rises to 68°C.

$$\xi Q_{\mathrm{LiOH}} + (1-\xi)\,Q_{\mathrm{water}} = C_{\mathrm{Li-Sol}}\,V_{\mathrm{Li-Sol}}\,\Delta T_{\mathrm{Li-Sol}} + C_{\mathrm{PTFE}}\,V_{\mathrm{PTFE}}\,\Delta T_{\mathrm{PTFE}}$$

On the basis of the equation and the numerical values listed above, with Q_{water} = 0.232 kJ ml^{-1}, and the volume percentage of LiOH in the solution ξ = 8.77%, we estimate the heat converted by LiOH as 1.268 kJ ml^{-1} or 20.79 kJ mol^{-1}.

With a similar equation

$$\xi Q_{\mathrm{NMCOH}} + (1-\xi)\,Q_{\mathrm{water}} = C_{\mathrm{NMC-H2O}}V_{\mathrm{NMC-H2O}}\,\Delta T_{\mathrm{NMC-H2O}} + C_{\mathrm{PTFE}}V_{\mathrm{PTFE}}\,\Delta T_{\mathrm{PTFE}}$$

and by using the specific heat of $Ni(OH)_2$ ($C_{\mathrm{Ni(OH)2}}$ = 82 J K^{-1} mol^{-1}) as that of NMCOH (C_{NMCOH}) (*80*), the volume specific heat of the mixture of water and NMCOH ($C_{\mathrm{NMC\text{-}H2O}}$) is derived as 3.86 J K^{-1} ml^{-1} by combining the density (3.652 g ml^{-1}) and molar mass (91.54 g mol^{-1}) of NMCOH. The volume percentage of NMCOH ξ is 35.34%. The temperature variations for the mixture and PTFE ($\Delta T_{\mathrm{NMC\text{-}H2O}}$ and ΔT_{PTFE}) are 73° and 46°C, respectively, as the temperature rises to 96°C. Therefore, the heat converted by NMCOH should be 34.58 kJ mol^{-1}.

SUPPLEMENTARY MATERIALS

Supplementary material for this article is available at http://advances.sciencemag.org/cgi/content/full/6/51/eabd9472/DC1

REFERENCES AND NOTES

1. C. Wang, W. Ping, Q. Bai, H. Cui, R. Hensleigh, R. Wang, A. H. Brozena, Z. Xu, J. Dai, Y. Pei, C. Zheng, G. Pastel, J. Gao, X. Wang, H. Wang, J.-C. Zhao, B. Yang, X. R. Zheng, J. Luo, Y. Mo, B. Dunn, L. Hu, A general method to synthesize and sinter bulk ceramics in seconds. *Science* **368**, 521–526 (2020).
2. J. R. Welty, C. E. Wicks, R. E. Wilson, *Fundamentals of Momentum, Heat, and Mass Transfer* (Wiley, ed. 2, 1976).
3. J. H. I. Lienhard, J. H. V. Lienhard, *A Heat Transfer Textbook* (Dover Publications, ed. 5, 2019).
4. A. K. Bhattacharya, Temperature-enthalpy approach to the modelling of self-propagating combustion synthesis of materials. *J. Mater. Sci.* **27**, 3050–3061 (1992).
5. A. A. Markov, I. A. Filimonov, Modeling of thermal radiation during zinc sulfide synthesis via combustion in a wet inert gas environment. *AIP Conf. Proc.* **2181**, 020012 (2019).
6. E. J. Horn, B. R. Rosen, Y. Chen, J. Z. Tang, K. Chen, M. D. Eastgate, P. S. Baran, Scalable and sustainable electrochemical allylic C–H oxidation. *Nature* **533**, 77–81 (2016).
7. A. Badalyan, S. S. Stahl, Cooperative electrocatalytic alcohol oxidation with electron-proton-transfer mediators. *Nature* **535**, 406–410 (2016).
8. R. S. Sherbo, R. S. Delima, V. A. Chiykowski, B. P. MacLeod, C. P. Berlinguette, Complete electron economy by pairing electrolysis with hydrogenation. *Nat. Catal.* **1**, 501–507 (2018).
9. P. Wang, S. Tang, P. F. Huang, A. W. Lei, Electrocatalytic oxidant-free dehydrogenative C–H/S–H cross-coupling. *Angew. Chem. Int. Ed.* **56**, 3009–3013 (2017).
10. M. Cologna, B. Rashkova, R. Raj, Flash sintering of nanograin zirconia in <5 s at 850 °C. *J. Am. Ceram. Soc.* **93**, 3556–3559 (2010).
11. L. A. Perez-Maqueda, E. Gil-Gonzalez, M. A. Wassel, S. K. Jha, A. Perejon, H. Charalambous, J. Okasinski, P. E. Sanchez-Jimenez, T. Tsakalakos, Insight into the $BiFeO_3$ flash sintering process by in-situ energy dispersive X-ray diffraction (ED-XRD). *Ceram. Int.* **45**, 2828–2834 (2019).
12. L. A. Malone, P. Qian, G. E. Mayneord, A. Hitchcock, D. A. Farmer, R. F. Thompson, D. J. K. Swainsbury, N. A. Ranson, C. N. Hunter, M. P. Johnson, Cryo-EM structure of the spinach cytochrome b_6f complex at 3.6 Å resolution. *Nature* **575**, 535–539 (2019).
13. X. Zhu, Y. Lin, J. San Martin, Y. Sun, D. Zhu, Y. Yan, Lead halide perovskites for photocatalytic organic synthesis. *Nat. Commun.* **10**, 2843 (2019).
14. D. M. Schultz, T. P. Yoon, Solar synthesis: Prospects in visible light photocatalysis. *Science* **343**, 1239176 (2014).

15. D. Friedmann, A. Hakki, H. Kim, W. Choic, D. Bahnemannd, Heterogeneous photocatalytic organic synthesis: State-of-the-art and future perspectives. *Green Chem.* **18**, 5391–5411 (2016).
16. C. Xu, P. R. Anusuyadevi, C. Aymonier, R. Luque, S. Marre, Nanostructured materials for photocatalysis. *Chem. Soc. Rev.* **48**, 3868–3902 (2019).
17. S. Shanmugam, C. Boyer, Organic photocatalysts for cleaner polymer synthesis. *Science* **352**, 1053–1054 (2016).
18. M. J. Collins Jr., Future trends in microwave synthesis. *Future Med. Chem.* **2**, 151–155 (2010).
19. N. R. Council, *Microwave Processing of Materials* (The National Academies Press, 1994).
20. P. Lidstrom, J. Tierney, B. Wathey, J. Westman, Microwave assisted organic synthesis—A review. *Tetrahedron* **57**, 9225–9283 (2001).
21. C. O. Kappe, Controlled microwave heating in modern organic synthesis. *Angew. Chem. Int. Ed.* **43**, 6250–6284 (2004).
22. A. de la Hoz, A. Díaz-Ortiz, A. Moreno, Microwaves in organic synthesis. Thermal and non-thermal microwave effects. *Chem. Soc. Rev.* **34**, 164–178 (2005).
23. A. de la Hoz, A. Díaz-Ortiz, A. Moreno, Review on non-thermal effects of microwave irradiation in organic synthesis. *J. Microw. Power Electromagn. Energy* **41**, 45–66 (2007).
24. S. Kawashima, M. Nishida, I. Ueda, H. Ouchi, $Ba(Zn_{1/3}Ta_{2/3})O_3$ ceramics with low dielectric loss at microwave-frequencies. *J. Am. Ceram. Soc.* **66**, 421–423 (1983).
25. I. M. Reaney, D. Iddles, Microwave dielectric ceramics for resonators and filters in mobile phone networks. *J. Am. Ceram. Soc.* **89**, 2063–2072 (2006).
26. R. Nicula, M. Stir, K. Ishizaki, J. M. Catala-Civera, S. Vaucher, Nanocrystallization of amorphous alloys using microwaves: In situ time-resolved synchrotron radiation studies. *J. Phys. Conf. Ser.* **144**, 012109 (2009).
27. R. Nicula, M. Stir, K. Ishizaki, J. M. Catala-Civera, S. Vaucher, Rapid nanocrystallization of soft-magnetic amorphous alloys using microwave induction heating. *Scr. Mater.* **60**, 120–123 (2009).
28. M. Taddei, N. Casati, D. A. Steitz, K. C. Dümbgen, J. A. van Bokhoven, M. Ranocchiari, In situ high-resolution powder x-ray diffraction study of UiO-66 under synthesis conditions in a continuous-flow microwave reactor. *CrystEngComm.* **19**, 3206–3214 (2017).
29. M. B. Gawande, S. N. Shelke, R. Zboril, R. S. Varma, Microwave-assisted chemistry: Synthetic applications for rapid assembly of nanomaterials and organics. *Acc. Chem. Res.* **47**, 1338–1348 (2014).
30. X. Ouyang, P. Cao, S. F. Huang, W. J. Zhang, Z. H. Huang, W. Gao, Microwave-assisted synthesis of high dielectric constant $CaCu_3Ti_4O_{12}$ from sol–gel precursor. *J. Electron. Mater.* **44**, 2243–2249 (2015).
31. J. Xin, J. Yang, S. Li, A. Basit, B. Sun, S. Li, Q. Long, X. Li, Y. Chen, Q. Jiang, Thermoelectric performance of rapidly microwave-synthesized α-MgAgSb with SnTe nanoinclusions. *Chem. Mater.* **31**, 2421–2430 (2019).
32. E. S. Reddy, S. Sukumaran, K. C. J. Raju, Microwave assisted synthesis, sintering of lead-free ferroelectric $CaBi_4Ti_4O_{15}$ ceramics. *Mater. Today Proc.* **3**, 2213–2219 (2016).
33. N. Sabelstrom, M. Hayashi, T. Watanabe, K. Nagata, Observation of localized heating phenomena during microwave heating of mixed powders using in situ x-ray diffraction technique. *J. Appl. Phys.* **116**, 164902 (2014).
34. J. S. Schanche, Microwave synthesis solutions from personal chemistry. *Mol. Divers.* **7**, 293–300 (2003).
35. N. Nakamura, L. Su, J. Bai, S. Ghose, B. Reeja-Jayan, In situ synchrotron pair distribution function analysis to monitor synthetic pathways under electromagnetic excitation. *J. Mater. Chem. A* **8**, 15909–15918 (2020).
36. K.-S. Lee, S.-T. Myung, Y.-K. Sun, Microwave synthesis of spherical $Li[Ni_{0.4}Co_{0.2}Mn_{0.4}]O_2$ powders as a positive electrode material for lithium batteries. *Chem. Mater.* **19**, 2727–2729 (2007).
37. J. Wang, M. H. Zhang, C. L. Tang, Y. G. Xia, Z. P. Liu, Microwave-irradiation synthesis of $Li_{1.3}Ni_xCo_yMn_{1-x-y}O_{2.4}$ cathode materials for lithium ion batteries. *Electrochim. Acta* **80**, 15–21 (2012).
38. Y. Tokura, N. Nagaosa, Orbital physics in transition-metal oxides. *Science* **288**, 462–468 (2000).
39. S. V. Kalinin, N. A. Spaldin, Functional ion defects in transition metal oxides. *Science* **341**, 858–859 (2013).
40. J. Suntivich, K. J. May, H. A. Gasteiger, J. B. Goodenough, Y. Shao-Horn, A perovskite oxide optimized for oxygen evolution catalysis from molecular orbital principles. *Science* **334**, 1383–1385 (2011).
41. C. N. R. Rao, A. K. Cheetham, Giant magnetoresistance in transition metal oxides. *Science* **272**, 369–370 (1996).
42. G. Chen, W. Zhou, D. Guan, J. Sunarso, Y. Zhu, X. Hu, W. Zhang, Z. Shao, Two orders of magnitude enhancement in oxygen evolution reactivity on amorphous $Ba_{0.5}Sr_{0.5}Co_{0.8}Fe_{0.2}O_{3-\delta}$ nanofilms with tunable oxidation state. *Sci. Adv.* **3**, e1603206 (2017).
43. K. Mizushima, P. C. Jones, P. J. Wiseman, J. B. Goodenough, Li_xCoO_2 (0<x<1): A new cathode material for batteries of high-energy density. *Mater. Res. Bull.* **15**, 783–789 (1980).
44. Y. Shao-Horn, L. Croguennec, C. Delmas, E. C. Nelson, M. A. O'Keefe, Atomic resolution of lithium ions in $LiCoO_2$. *Nat. Mater.* **2**, 464–467 (2003).
45. Z. Wu, S. Ji, J. Zheng, Z. Hu, S. Xiao, Y. Wei, Z. Zhuo, Y. Lin, W. Yang, K. Xu, K. Amine, F. Pan, Prelithiation activates $Li(Ni_{0.5}Mn_{0.3}Co_{0.2})O_2$ for high capacity and excellent cycling stability. *Nano Lett.* **15**, 5590–5596 (2015).
46. M. M. Thackeray, C. Wolverton, E. D. Isaacs, Electrical energy storage for transportation-approaching the limits of, and going beyond, lithium-ion batteries. *Energy Environ. Sci.* **5**, 7854–7863 (2012).
47. J. M. Tarascon, M. Armand, Issues and challenges facing rechargeable lithium batteries. *Nature* **414**, 359–367 (2001).
48. T. C. Liu, F. Pan, K. Amine, Prospect and reality of concentration gradient cathode of lithium-ion batteries. *Chin. J. Struct. Chem.* **39**, 11–15 (2020).
49. Z.-W. Yin, J.-T. Li, L. Huang, F. Pan, S.-G. Sun, High-capacity Li-rich Mn-based cathodes for lithium-ion batteries. *Chin. J. Struct. Chem.* **39**, 20–25 (2020).
50. M.-J. Zhang, G. F. Teng, Y.-C. K. Chen-Wiegart, Y. Duan, J. Y. P. Ko, J. X. Zheng, J. Thieme, E. Dooryhee, Z. Chen, J. Bai, K. Amine, F. Pan, F. Wang, Cationic ordering coupled to reconstruction of basic building units during synthesis of high-Ni layered oxides. *J. Am. Chem. Soc.* **140**, 12484–12492 (2018).
51. K. Kang, Y. S. Meng, J. Breger, C. P. Grey, G. Ceder, Electrodes with high power and high capacity for rechargeable lithium batteries. *Science* **311**, 977–980 (2006).
52. K. Kang, G. Ceder, Factors that affect Li mobility in layered lithium transition metal oxides. *Phys. Rev. B* **74**, 094105 (2006).
53. Y. Wei, J. Zheng, S. Cui, X. Song, Y. Su, W. Deng, Z. Wu, X. Wang, W. Wang, M. Rao, Y. Lin, C. Wang, K. Amine, F. Pan, Kinetics tuning of Li-ion diffusion in layered $Li(Ni_xMn_yCo_z)O_2$. *J. Am. Chem. Soc.* **137**, 8364–8367 (2015).
54. S. Cui, Y. Wei, T. Liu, W. Deng, Z. Hu, Y. Su, H. Li, M. Li, H. Guo, Y. Duan, W. Wang, M. Rao, J. Zheng, X. Wang, F. Pan, Optimized temperature effect of Li-ion diffusion with layer distance in $Li(Ni_xMn_yCo_z)O_2$ cathode materials for high performance Li-ion battery. *Adv. Energy Mater.* **6**, 1501309 (2016).
55. Z.-Y. Li, R. Gao, J. Zhang, X. Zhang, Z. Hu, X. Liu, New insights into designing high-rate performance cathode materials for sodium ion batteries by enlarging the slab-spacing of the Na-ion diffusion layer. *J. Mater. Chem. A* **4**, 3453–3461 (2016).
56. R. Xu, Y. Xu, *Modern Inorganic Synthetic Chemistry* (Elsevier, ed. 2, 2017).
57. J. Sun, W. Wang, Q. Yue, Review on microwave-matter interaction fundamentals and efficient microwave-associated heating strategies. *Materials* **9**, 231 (2016).
58. A. Samanta, R. W. Fessenden, Excited-state dipole moment of 7-aminocoumarins as determined from time-resolved microwave dielectric absorption measurements. *J. Phys. Chem. A* **104**, 8577–8582 (2000).
59. E. R. Kasimov, M. A. Sadykhov, R. M. Kasimov, C. O. Kadzhar, Measurement of dielectric properties of high-absorption materials at microwave frequencies. *Meas. Tech.* **42**, 475–478 (1999).
60. Z. Wu, K. Pei, L. Xing, X. Yu, W. You, R. Che, Enhanced microwave absorption performance from magnetic coupling of magnetic nanoparticles suspended within hierarchically tubular composite. *Adv. Funct. Mater.* **29**, 1901448 (2019).
61. J. Zhou, W. Xu, Z. You, Z. Wang, Y. Luo, L. Gao, C. Yin, R. Peng, L. Lan, A new type of power energy for accelerating chemical reactions: The nature of a microwave-driving force for accelerating chemical reactions. *Sci. Rep.* **6**, 25149 (2016).
62. J. Ludwig, C. Marino, D. Haering, C. Stinner, D. Nordlund, M. M. Doeff, H. A. Gasteiger, T. Nilges, Facile, ethylene glycol-promoted microwave-assisted solvothermal synthesis of high-performance $LiCoPO_4$ as a high-voltage cathode material for lithium-ion batteries. *RSC Adv.* **6**, 82984–82994 (2016).
63. K. J. Kreder, G. Assat, A. Manthiram, Microwave-assisted solvothermal synthesis of three polymorphs of $LiCoPO_4$ and their electrochemical properties. *Chem. Mater.* **27**, 5543–5549 (2015).
64. D. J. Miller, J. M. Lisy, Entropic effects on hydrated alkali-metal cations: Infrared spectroscopy and ab initio calculations of $M^+(H_2O)_{x=2-5}$ cluster ions for M = Li, Na, K, and Cs. *J. Am. Chem. Soc.* **130**, 15393–15404 (2008).
65. D. J. Miller, J. M. Lisy, Hydrated alkali-metal cations: Infrared spectroscopy and ab initio calculations of $M^+(H_2O)_{x=2-5}Ar$ cluster ions for M = Li, Na, K, and Cs. *J. Am. Chem. Soc.* **130**, 15381–15392 (2008).
66. E. S. Boek, P. V. Coveney, N. T. Skipper, Monte Carlo molecular modeling studies of hydrated Li-, Na-, and K-smectites: Understanding the role of potassium as a clay swelling inhibitor. *J. Am. Chem. Soc.* **117**, 12608–12617 (1995).
67. J. Hu, W. Li, Y. Duan, S. Cui, X. Song, Y. Liu, J. Zheng, Y. Lin, F. Pan, Single-particle performances and properties of $LiFePO_4$ nanocrystals for Li-ion batteries. *Adv. Energy Mater.* **7**, 1601894 (2017).
68. J. Zheng, Y. Hou, Y. Duan, X. Song, Y. Wei, T. Liu, J. Hu, H. Guo, Z. Zhuo, L. Liu, Z. Chang, X. Wang, D. Zherebetskyy, Y. Fang, Y. Lin, K. Xu, L.-W. Wang, Y. Wu, F. Pan, Janus solid–liquid interface enabling ultrahigh charging and discharging rate for advanced lithium-ion batteries. *Nano Lett.* **15**, 6102–6109 (2015).

69. C. O. Kappe, B. Pieber, D. Dallinger, Microwave effects in organic synthesis: Myth or reality? *Angew. Chem. Int. Ed.* **52**, 1088–1094 (2013).
70. K. Nushiro, S. Kikuchi, T. Yamada, Microwave effect on catalytic enantioselective Claisen rearrangement. *Chem. Commun.* **49**, 8371–8373 (2013).
71. M. R. Rosana, Y. Tao, A. E. Stiegman, G. B. Dudley, On the rational design of microwave-actuated organic reactions. *Chem. Sci.* **3**, 1240–1244 (2012).
72. J. Niu, R. Shao, J. Liang, M. Dou, Z. Li, Y. Huang, F. Wang, Biomass-derived mesopore-dominant porous carbons with large specific surface area and high defect density as high performance electrode materials for Li-ion batteries and supercapacitors. *Nano Energy* **36**, 322–330 (2017).
73. W. Zhang, M. Topsakal, C. Cama, C. J. Pelliccione, H. Zhao, S. Ehrlich, L. Wu, Y. Zhu, A. I. Frenkel, K. J. Takeuchi, E. S. Takeuchi, A. C. Marschilok, D. Lu, F. Wang, Multi-stage structural transformations in zero-strain lithium titanate unveiled by in situ X-ray absorption fingerprints. *J. Am. Chem. Soc.* **139**, 16591–16603 (2017).
74. D. Wang, R. Kou, Y. Ren, C.-J. Sun, H. Zhao, M.-J. Zhang, Y. Li, A. Huq, J. Y. Peter Ko, F. Pan, Y.-K. Sun, Y. Yang, K. Amine, J. Bai, Z. Chen, F. Wang, Synthetic control of kinetic reaction pathway and cationic ordering in high-Ni layered oxide cathodes. *Adv. Mater.* **29**, 1606715 (2017).
75. J. Chen, J. Bai, H. Chen, J. Graetz, In situ hydrothermal synthesis of $LiFePO_4$ studied by synchrotron x-ray diffraction. *J. Phys. Chem. Lett.* **2**, 1874–1878 (2011).
76. M.-J. Zhang, Y.-S. Chen, F. Pan, Y. Ren, Understanding structural evolution in the synthesis of advanced energy materials. *Chin. J. Struct. Chem.* **39**, 26–30 (2020).
77. The Engineering ToolBox, www.engineeringtoolbox.com/specific-heat-capacity-d_391.html.
78. P. J. Gierszewski, R. C. Prasad, D. W. Kirk, Properties of LiOH and $LiNO_3$ aqueous-solutions: Additional results. *Fusion Eng. Des.* **15**, 279–283 (1992).
79. P. J. Gierszewski, P. A. Finn, D. W. Kirk, Properties of LiOH and $LiNO_3$ aqueous-solutions. *Fusion Eng. Des.* **13**, 59–71 (1990).
80. H. Gamsjäger, F. J. Mompean, Chemical thermodynamics, in *Chemical Thermodynamics of Nickel* (Elsevier, 2005).

Acknowledgments: We thank N. Nakamura and B. Reeja Jayan for their contributions to the idea and J. Trunk and S. Bennett for their technical assistance in the reengineering of the MW reactor. **Funding:** This work was supported by the U.S. Department of Energy (DOE) Office of Energy Efficiency and Renewable Energy, Vehicle Technologies Office, contract no. DE-SC0012704, and National Key R&D Program of China (2016YFB0700600). This research used 28-ID-1 (PDF) and 28-ID-2 (XPD) beamline at the National Synchrotron Light Source II, a U.S. DOE Office of Science User Facility operated for the DOE Office of Science by Brookhaven National Laboratory under contract no. DE-SC0012704. K.X. thanks the Joint Center for Energy Storage Research, an Energy Innovation Hub funded by the U.S. Department of Energy, Office of Science, Basic Energy Sciences through IAA SN2020957. F.P. thanks the support from Guangdong innovative team program (2013 N080), Soft Science Research Project of Guangdong Province (no. 2017B030301013), and Shenzhen Science and Technology Research Grant (ZDSYS201707281026184). **Author contributions:** J.B., F.W., F.P., and K.X. designed and supervised the research. J.B., H.Z., and E.D., with contributions from M.-J.Z. and F.W., designed and fabricated the MW reaction cell. M.-J.Z. conducted in situ MW, in situ hydrothermal, and in situ solid-state experiments with the help of Y.D., C.Y., and H.Z. M.L. performed the morphology characterization. All authors discussed the results and contributed to manuscript preparation. **Competing interests:** The authors declare that they have no competing interests. **Data and materials availability:** All data needed to evaluate the conclusions in the paper are present in the paper and/or the Supplementary Materials. Additional data related to this paper may be requested from the authors.

Submitted 26 July 2020
Accepted 4 November 2020
Published 16 December 2020
10.1126/sciadv.abd9472

Citation: M.-J. Zhang, Y. Duan, C. Yin, M. Li, H. Zhong, E. Dooryhee, K. Xu, F. Pan, F. Wang, J. Bai, Ultrafast solid-liquid intercalation enabled by targeted microwave energy delivery. *Sci. Adv.* **6**, eabd9472 (2020).